Arch Appl Mech (2016) 86:335–349
DOI 10.1007/s00419-015-1107-3

SPECIAL

Christoph Settgast · Martin Abendroth · Meinhard Kuna

Fracture mechanical analysis of open cell ceramic foams under multi-axial mechanical loading

Received: 24 August 2015 / Accepted: 18 November 2015 / Published online: 12 January 2016

Abstract Ceramic foams made by replica techniques contain sharp edged cavities, which are potential crack initiators. This paper presents an approach to analyse such structures with respect to their fracture mechanical properties. A fundamental domain of an open cell Kelvin foam is used to model the geometry including the cavities and to generate a finite element model of the structure. Sub-models containing crack tip elements are used to resolve the local stress fields at the vicinity of the sharp-edged cavities. The interaction integral is used to compute the local stress intensity factors under multi-axial loading. Using a homogenization approach, a criterion for brittle failure based on the effective stress state is presented. The failure criteria can be extended to account for the anisotropic behaviour of the foam structure.

Keywords Fracture criteria · Stress intensity factors · Multi axial loading · Kelvin foam · Ceramic foam

1 Introduction

Open cell ceramic foams are widely used in industrial processes, e.g. as filters for metal casting, as catalysts or as burner plates in furnaces. One of the production routes of such foams is the Schwartzwalder process [1], where an open cell polyurethane (PU) foam, see Fig. 1 middle, is coated with a ceramic slurry, dried and finally fired. During the firing process, the PU pyrolyses and sharp-edged cavities remain, see Fig. 1 left. Cracks may initiate at the edges of these cavities under external loading. The properties of ceramic foams have been analysed in many studies. Colombo and Hellmann [2] describe fabrication processes and their influence on the mechanical properties of reticulated ceramic foams. Twigg and Richardson [3] studied heat transfer and transport properties of ceramic foam catalysts. Gibson and Ashby [4] derived fundamental theoretical basics to describe the mechanical behaviour of foams.

Jang, Kraynik and Kyriakides studies the microstructure of open cell foams and its effects on the elastic properties [5]. Detailed numerical models of open cell foams where developed by Kraynik et al. [6] using the surface evolver of Ken Brakke [7] to analyse the mechanical behaviour. Storm et al. [8] developed a novel modelling strategy for open cell foams based on implicit functions and studied the influence of basic geometrical properties on the mechanical and thermal properties.

The open cell Kelvin foam [9] is often used as a simplified model [10–13]. Analytical description of the mechanical behaviour is given by Zhu et al. [14] and also by Warren and Kraynik [15].

Failure of open cell ceramic foams are described by various failure criteria [16–18].

To the authors knowledge the sharp-edged cavities of reticulated open cell ceramic foams which may act as crack initiators have not been analysed so far. We describe in detail the development of a finite element model, which takes into account the foam productions process.

C. Settgast (✉) · M. Abendroth · M. Kuna
TU Bergakademie Freiberg, Institute for Mechanics and Fluid Dynamics, Lampadiusstraße 4, 09596 Freiberg, Germany
E-mail: Christoph.Settgast@imfd.tu-freiberg.de

This paper presents a procedure how to evaluate the integrity of those foams in terms of fracture toughness as well as classical strength hypothesis. This evaluation is applied for selected examples and parameters.

2 Models and methods

2.1 Finite element model generation

To generate a finite element foam model, we perform the following procedure. First, a periodic close hard sphere packing is created using a molecular dynamics code of Skoge et al. [19]. Using the centre points of the spheres, the corresponding Voronoi tessellation is computed with help of Rycroft's Voronoi cell library [20]. The Voronoi tessellation is then converted into a Surface Evolver model, because the Voronoi tessellation is not the structure with a locally stable energy minimum. Such a structure is found using the Surface Evolver [7], which minimizes the surface area and therewith the surface energy of the whole foam. During the minimization several topological changes have to be made, if single facets or edges shrink to a single point. Kraynik et al. [6] implemented algorithms, which take care of such situations. The result may then be a foam as shown in the left picture in Fig. 2. The surface evolver also allows to generate the corresponding wet foam, where each triple edge of the foam is converted into a plateau border. At this step it is possible to chose the volume of the liquid phase of the wet foam. The relaxed state of the wet foam without its cell walls is taken as the geometry of the PU foam (see Fig. 1 right). This geometry represents the inner surface of the ceramic foam, where all triple edges are the sharp edges of the cavities. To model the coating the same evolver mesh is used, but all triple edges of the wet foam are taken as inner constraints for the coating surface. Now the coating volume can be defined and outer surface is computed. This surface is still spanned tightly over the triple edge constraints, whereas a second coating step is applied, which is defined by an equidistant surface. This procedure follows

Fig. 1 Broken ceramic foam, polyurethane foam, surface evolver [7] model of a wet Kelvin foam

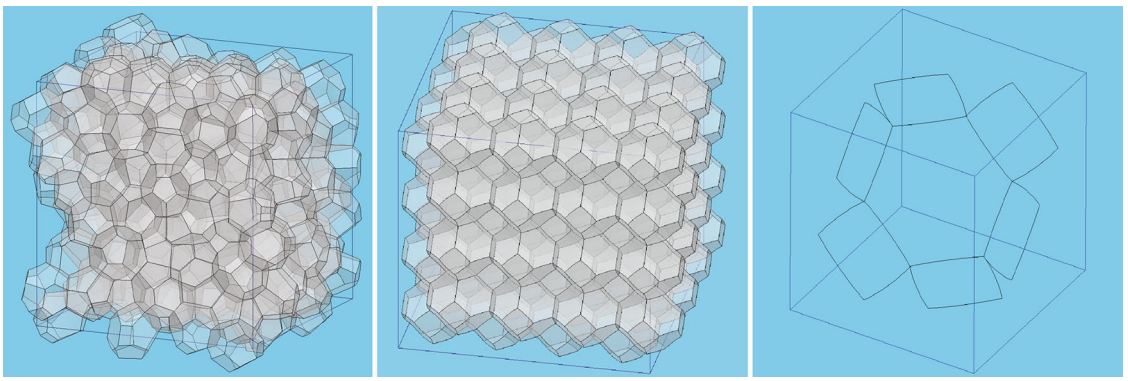

Fig. 2 Evolver models of periodic monodispersed foams. (*Left*) Relaxed random foam based on a sphere packing. (*Centre*) BCC lattice of a relaxed Kelvin foam. (*Right*) The corresponding strut network of a Kelvin soap foam. The foam struts are defined as the Plateau borders, where three cell walls met at dihedral angles of $\arccos(-1/2) = 120°$. Foam nodes are located where four Plateau borders (struts) met, which are slightly curved and met at tetrahedral angles of $\arccos(-1/3) \approx 109.47°$

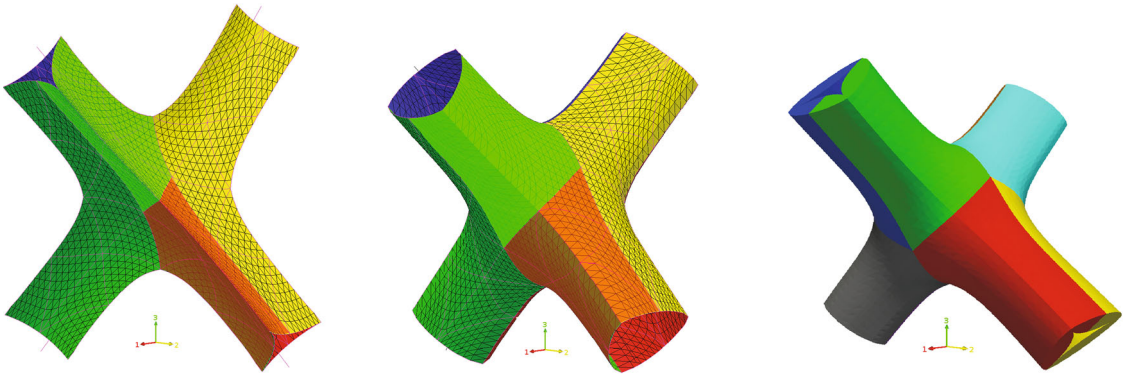

Fig. 3 (*Left*) Wet foam model of a single Kelvin cell node with a fundamental domain (*green*) and a domain (*red*) get by a rotation of π around the (110)-axis. The cell walls still exist but are not displayed. (*Middle*) Same structure with a liquid coating with the same two domains (*orange* and *green*). (*Right*) Volume model as a combination of the inner and outer surfaces. *Different colours* show the different domains. (Color figure online)

the steps of the real coating process, where the PU foam is first drained with a slurry, then dried and followed by a second spray coating process. It would be also possible to repeat the spray coating to generate a second coating, which could even represent a separate material.

All the steps can be done for a stochastic foam (see Fig. 2 left) as well, but for the sake of clarity we concentrate on a crystalline Kelvin foam (see Fig. 2 centre), where a body centre cubic (BCC) arrangement of cells is representative for the whole foam. For a stochastic foam containing thousands of cells, the first three steps of this procedure can be a time consuming and laborious process.

Figure 2 (right) shows a representative volume element (RVE) of a Kelvin foam. It is already in its relaxed state. For the picture, all foam faces have been removed only the struts remain. This structure still has threefold rotation symmetries around the cube diagonals as well as fourfold rotation symmetries around the normals through the centres of all quadrangles. Therefore, we simplify the structure further and end up with a single node, where four struts met. This geometry is enclosed by symmetry planes, which are normal to the four struts axes forming a tetrahedron. There are still two more mirror symmetry planes with normals in 1- and 2-direction, which are not used here. The fundamental domain of the structure is highlighted in Fig. 3 (left and middle) by an orange colour. The green domain is created by a rotation by π around the (111)-axes. All other domains may be created by mirror operations.

Figure 3 (left) shows the relaxed wet foam evolver model of a single Kelvin cell node. The liquid volume fraction for a whole RVE (as in Fig. 2 right) is 0.7 %. This structure now serves as an assumed rigid foam, which gets a simulated coating in two steps. In the first coating step, a liquid layer is computed using the surface evolver again forming a minimal surface. The six sharp edges of the wet foam are used as inner wire constraints where the slurry surface is spanned over. The volume of the liquid can be defined. The second coating is a layer of constant thickness over the total outer surface. This state is shown in the middle of Fig. 3. The inner and outer surfaces represent the lower and upper boundary surface of a single volume, which is finally used to create a finite element (FE) mesh, see Fig. 3 (right). The surfaces are approximated by bivariate cubic splines. The node is generated by mirror and rotation operations of one fundamental domain, see the different colours in Fig. 3 (right). Six complete nodes and twelve half nodes finally form the Kelvin cell foam model containing the sharp-edged cavities. It is still an idealized structure because the liquid coating process is computed without considering external forces like gravity and any motion of the structure within an environment. But the form of the node which is significantly thicker than the struts is very realistic.

Figure 4 (left) shows the final FE model of Kelvin cell having a relative density of 3.8 %, which can be adjusted by choosing different volumes for the initial wet foam and the first coating and another thickness of the second coating. The whole Kelvin cell is generated from the fundamental domain with reflections, rotations and translations, see the different colours in Fig. 4 (left).

For evaluating stress intensity factors (SIF) along the cavity corners submodels are created, which are circular crack tip meshes (see Fig. 4 right) extruded along the edges of the cavities. There exist three submodels for the four-sided strut loops around the normals (100), (010) and (001). For the six-sided strut loops, another four submodels are used having the normals (111), (11-1), (1-11) and (-111) as depicted in Fig. 5. For each submodel a local parametric coordinate (lpc) is introduced which goes from [0…4] for a four-sided strut loop

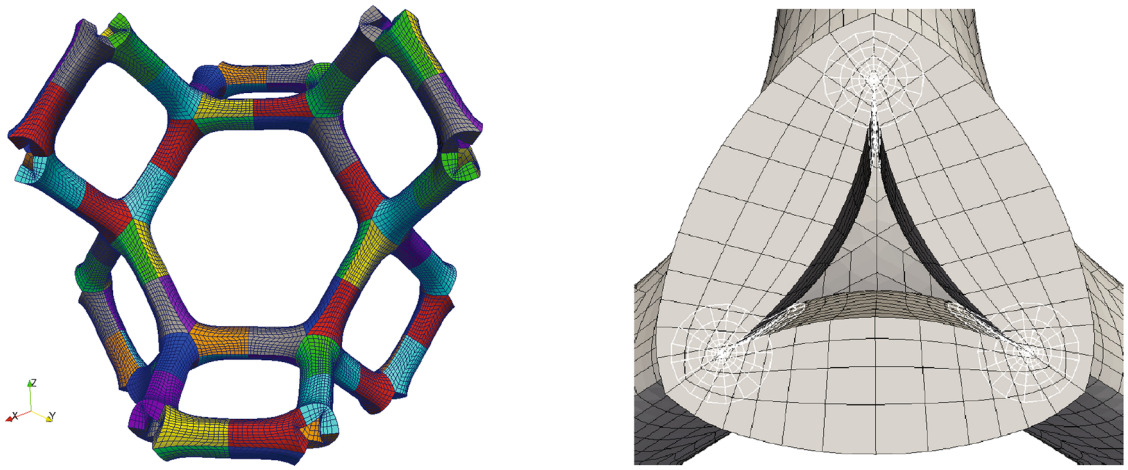

Fig. 4 (*Left*) Finite element model of the Kelvin foam including the sharp edged strut cavities with different domains. (*Right*) Detail of the mesh (*black grid*) together with the submodels (*white grid*) for stress intensity factor calculations

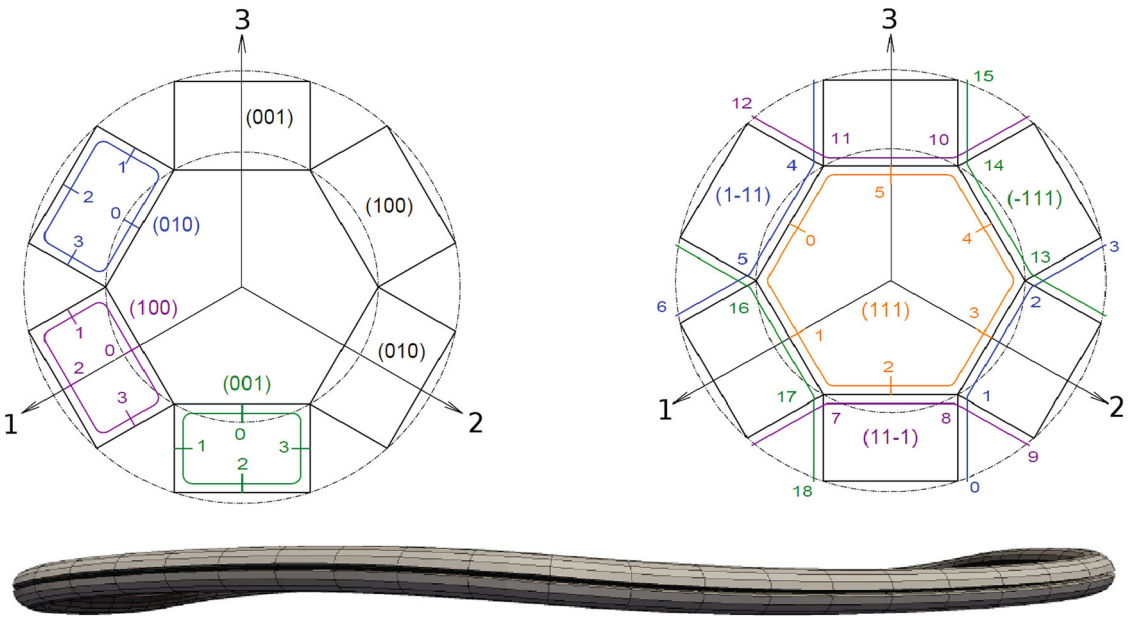

Fig. 5 Definitions for quadrilateral and hexagonal crack paths. (*Bottom*) A submodel for a hexagonal crack, the view is in plane of the hexagon so that the out of plane curvature can be seen clearly

and from [0...6] for a six-sided strut loop. An in plane view of the submodel around the normal (111) is also shown in Fig. 5 (bottom), where the out of plane curvature for the hexagonal submodel becomes visible.

For the simulations, the commercial FEM code Abaqus [21] is used. The material properties are for a Al_2O_3 ceramic with 95 % density [22,23]. The elastic modulus is $E = 320\,\text{GPa}$, Poisson's ratio $\nu = 0.25$, tensile fracture strength $\sigma_c = 300\,\text{MPa}$ and the mode I fracture toughness $K_{I_c} = 3.3\,\text{MPa}\sqrt{\text{m}}$. The size of the RVE is $2 \times 2 \times 2\,\text{mm}^3$.

2.2 Homogenization and external loading

Considering a linear elastic material and small deformation theory, the homogenization is analogous to Storm et al. [8]. Σ_{ij} and E_{ij} are the homogenized (effective) stresses and strains, which are the volume averages of the local stresses and strains σ_{ij} and ε_{ij}, with $i, j = 1, 2, 3$.

$$\Sigma_{ij} = \frac{1}{V}\int \sigma_{ij}\mathrm{d}V \tag{1}$$

$$E_{ij} = \frac{1}{V}\int \varepsilon_{ij}\mathrm{d}V \tag{2}$$

At the boundary of the RVE, periodic boundary conditions are applied. The microdisplacement field u_i is the superposition of a homogeneous macrodisplacement field $U_i = E_{ij}x_j$ and a local periodic displacement fluctuation field $\tilde{u}_i$:

$$u_i = E_{ij}x_j + \tilde{u}_i \tag{3}$$

Periodicity requires similar displacement fluctuations and antiperiodic tractions at corresponding points on opposite boundaries $j-$ and $j+$.

$$\tilde{u}_i^{j-} = \tilde{u}_i^{j+} \tag{4}$$

$$t_i^{j-} = -t_i^{j+}. \tag{5}$$

The lower index describes the direction of the displacement or traction force and the upper index $j-$ or $j+$ the negative or positive surface of the RVE having a normal in j-direction. So the periodic displacement boundary conditions are applied using equation constraints

$$u_i^{j+} - u_i^{j-} = \Delta u_i^j \tag{6}$$

and symmetry conditions

$$\Delta u_i^j = \Delta u_j^i, \tag{7}$$

which is analogous to Storm et al. [8] as well. The boundary conditions are either the external displacements Δu_i^j or the tractions t_i^j, which are applied at reference nodes (one for each spatial direction j) and related to the effective stresses or strains by

$$\Sigma_{ij} = \frac{t_i^j}{l_{\mathrm{RVE}}^2} \tag{8}$$

$$E_{ij} = \frac{\Delta u_i^j}{l_{\mathrm{RVE}}} \tag{9}$$

assuming a cubic RVE with length l_{RVE}.

Failure and yield criteria are often formulated in a cylindrical coordinate system with coordinates p, q and θ, where p corresponds to the hydrostatic pressure

$$p = -\frac{1}{3}\Sigma_{ii} \tag{10}$$

and q to the equivalent von Mises stress

$$q = \sqrt{\frac{3}{2}S_{ij}S_{ij}} \tag{11}$$

expressed by the deviatoric part of the stress tensor

$$S_{ij} = \Sigma_{ij} - \frac{1}{3}\Sigma_{kk}\delta_{ij}. \tag{12}$$

The angle θ is defined counterclockwise around the hydrostatic axis $(-p)$ starting from the projection of the Σ_1-axis onto the π-plane, which denotes a plane in principle stress space, where the hydrostatic pressure $p = 0$.

The effective principal stresses are related to the cylindrical coordinates by

$$\begin{bmatrix}\Sigma_1\\ \Sigma_2\\ \Sigma_3\end{bmatrix} = \begin{bmatrix}p\\ p\\ p\end{bmatrix} + \frac{2}{3}q\begin{bmatrix}\cos\theta\\ \cos\left(\theta - \frac{2\pi}{3}\right)\\ \cos\left(\theta + \frac{2\pi}{3}\right)\end{bmatrix}. \tag{13}$$

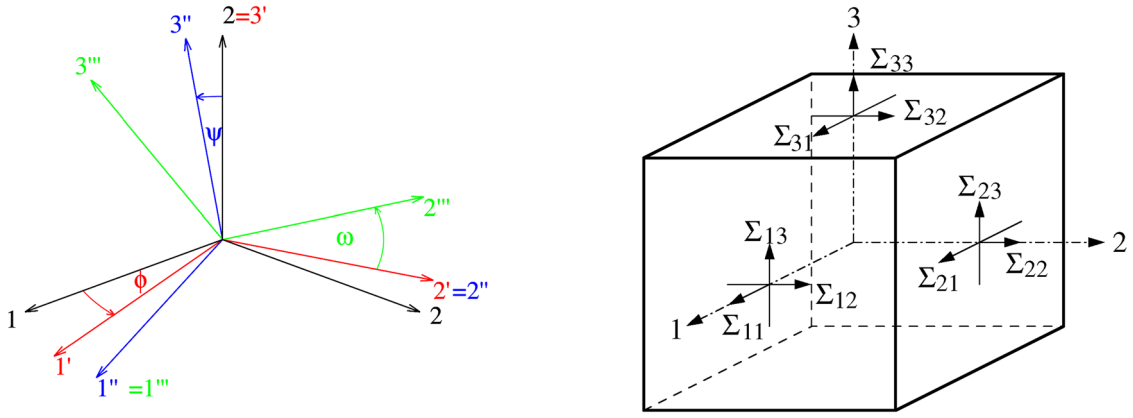

Fig. 6 Rotations for the stress state and general stress state

The response of the Kelvin cell on an external load also depends on the orientation of the stress state. The Kelvin cell is an orthotropic structure and obeys therefore all symmetries of the octahedral symmetry group (O_h). Hence, applying three subsequent rotations as shown in Fig. 6 (left) with ϕ around 3-axis, ψ around $2'$-axis and ω around $1''$ with

$$\phi \in \left[0, \frac{\pi}{4}\right] \tag{14}$$

$$\psi \in \left[0, \tan^{-1}\left(\frac{\tan\phi}{\sqrt{1+\tan^2\phi}}\right)\right] \tag{15}$$

$$\omega \in [0, \pi) \tag{16}$$

all representative stress states can be obtained. Consequently, the rotation matrix $R_{ik}(\phi, \psi, \omega)$ is

$$R_{ik}(\phi,\psi,\omega) = \begin{bmatrix} \cos\phi\cos\psi & \sin\phi\cos\psi & -\sin\psi \\ -\sin\phi\cos\omega + \cos\phi\sin\psi\sin\omega & \sin\phi\sin\psi\sin\omega + \cos\phi\cos\omega & \cos\psi\sin\omega \\ \sin\phi\sin\omega + \cos\phi\sin\psi\cos\omega & \sin\phi\sin\psi\cos\omega - \cos\phi\sin\omega & \cos\psi\cos\omega \end{bmatrix} \tag{17}$$

and the effective stress tensor is calculated by

$$\Sigma_{kl}(p,q,\theta,\phi,\psi,\omega) = \Sigma^{\mathrm{P}}_{ij}(p,q,\theta) R_{ik}(\phi,\psi,\omega) R_{jl}(\phi,\psi,\omega) \tag{18}$$

with

$$\Sigma^{\mathrm{P}}_{ij}(p,q,\theta) = \begin{bmatrix} \Sigma_1 & 0 & 0 \\ 0 & \Sigma_2 & 0 \\ 0 & 0 & \Sigma_3 \end{bmatrix} \tag{19}$$

and the principal values Σ_i from Eq. (13).

2.3 Local failure criteria

Two local stress-based measures are used to define local material loading. The first is the classical von Mises stress.

$$\sigma_{\mathrm{vM}} = \sqrt{\frac{1}{2} s_{ij} s_{ij}} \tag{20}$$

s_{ij} denotes the local deviatoric stress tensor. This measure is evaluated only for the outer surfaces of the foam.

Secondly a fracture mechanical measure is used. Since an arbitrary stress state will cause local mixed mode loading, the coplanar SIF

$$K_{\mathrm{co}} = \sqrt{K_{\mathrm{I}}^2 + K_{\mathrm{II}}^2 + \frac{1}{1-\nu} K_{\mathrm{III}}^2} \tag{21}$$

is used as local measure for brittle failure. For a homogeneous isotropic material, the SIFs K_N are related to the J-integral [24] by

$$J = K_N Y_{NM} K_M = \frac{1-\nu^2}{E}\left(K_{\mathrm{I}}^2 + K_{\mathrm{II}}^2\right) + \frac{1+\nu}{E} K_{\mathrm{III}}^2, \tag{22}$$

where Y_{NM} denotes the Irwin matrix, here for a homogeneous isotropic material, with $N, M = \mathrm{I}, \mathrm{II}, \mathrm{III}$.

$$Y_{NM} = \frac{1}{E}\begin{bmatrix} 1-\nu^2 & 0 & 0 \\ 0 & 1-\nu^2 & 0 \\ 0 & 0 & 1+\nu \end{bmatrix} \tag{23}$$

To separate the SIFs, the interaction integral is used. The SIFs and the interaction integral J_M^{int} are related by

$$K_N = Y_{NM}^{-1} J_M^{\mathrm{int}} \frac{1}{k_0}, \tag{24}$$

where K_N is the SIF for mode $N = \mathrm{I}, \mathrm{II}, \mathrm{III}$, Y_{NM}^{-1} the inverted Irwin matrix and k_0 a unit value SIF. The scalar value of the interaction integral J_N^{int} for mode N is defined as

$$J_N^{\mathrm{int}} = \lim_{\Gamma \to 0} \int_{\Gamma} M_{ij}^N n_i q_j \mathrm{d}\Gamma \tag{25}$$

with

$$M_{ij}^N = \sigma_{kl} \varepsilon_{kl}^N \delta_{ij} - \sigma_{kj} u_{k,i}^N - \sigma_{kj}^N u_{k,i}, \tag{26}$$

which superimposes the actual fields σ_{kj}, ε_{kl} and $u_{k,i}$ with auxiliary fields σ_{kj}^N, ε_{kl}^N and $u_{k,i}^N$. These auxiliary fields are the known near crack tip solutions for pure mode N loading causing a unit value SIF k_0.

2.4 Homogenized failure criteria and failure surfaces

A homogenized failure criterion for a single local point P is a function of the effective (homogenized) stress state

$$\Sigma_{ij} A_{ijkl}^P \Sigma_{kl} - 1 \geq 0, \tag{27}$$

where A_{ijkl}^P represents the failure tensor for a local point P, e.g. an integration point or a point at the crack front. Σ_{ij} is the effective stress state, as defined in equation (18), that fulfils

$$\lambda_{\mathrm{c}}(\Sigma_{ij}) = \frac{f_{\mathrm{c}}(\sigma_{ij})|_{\Sigma_{ij}}}{c} - 1 \geq 0, \tag{28}$$

where $f_{\mathrm{c}}(\sigma_{ij})$ represents one of the local stress-based measures Eqs. (20) or (21). The constant c stands for the corresponding critical values σ_{c} or $K_{\mathrm{I_c}}$.

Considering a linear problem where

$$\sigma_{ij}(\lambda \Sigma_{kl}) = \lambda \sigma_{ij}(\Sigma_{kl}) \tag{29}$$

we can scale Σ_{ij} to $\hat{\Sigma}_{ij}$ so that Eq. (28) fulfils exactly

$$\lambda_{\mathrm{c}}(\hat{\Sigma}_{ij}) = 0 \tag{30}$$

and then Eq. (27) fulfils

$$\hat{\Sigma}_{ij} A_{ijkl}^P \hat{\Sigma}_{kl} - 1 = 0, \tag{31}$$

which is an implicit function, describing an isosurface in the effective stress space. Due to the symmetry of the effective stress tensor $\hat{\Sigma}_{ij}$, the failure tensor A_{ijkl}^P has the same symmetries as the elasticity tensor C_{ijkl} (Hooke's law):

$$A_{ijkl}^P = A_{ijlk}^P = A_{jikl}^P = A_{klij}^P. \tag{32}$$

So in a general case A^P_{ijkl} has only 21 independent components, which can be calculated using

$$\sqrt{\sum_{m=1}^{N}\left(\hat{\Sigma}^{(m)}_{ij}A^P_{ijkl}\hat{\Sigma}^{(m)}_{kl}-1\right)^2}\rightarrow\min \tag{33}$$

for $N \geq 21$ linearly independent stress states to approximate the failure surface for all stress states that fulfil Eqs. (30) and (31). Considering a linear elastic problem, the calculation of the components of A^P_{ijkl} can be simplified to the solution of a system of 21 linear equations

$$\hat{\Sigma}^{(m)}_{ij}A^P_{ijkl}\hat{\Sigma}^{(m)}_{kl}-1=0,\qquad m=1,2,\ldots,21 \tag{34}$$

with 21 linearly independent stress states.

2.5 Using the structural symmetry of the Kelvin cell

It has been shown in the previous section that the Kelvin cell is build up by fundamental domains, which have all the same shape but different orientations. Let us define homologous points, which are points having the same local position within their domain. The orientation of the domains are defined by the symmetry group of the structure, which is in the case of the Kelvin cell the octahedral group (O_h) containing all transformation matrices T_{ij}. All T_{ij} are defined by rotation and mirror operations, but no translations. The transformation matrices are orthogonal matrices, so that

$$T_{ij}T_{jk}=\delta_{ik} \tag{35}$$

The local stress state of a point P is a function of the effective stress state

$$\sigma^P_{ij}=g(\Sigma_{ij}). \tag{36}$$

Considering a linear elastic problem this relation is defined by the linear mapping

$$\sigma^P_{ij}=B^P_{ijkl}\Sigma_{kl} \tag{37}$$

with the mapping tensor B^P_{ijkl} between the effective stress state and the local stress state of point P. The local stress states of two homologous points obey the symmetries of the structure. To show this, we consider two homologous points P_1 and P_2. Using Eq. (37) we can write

$$\sigma^{P_1}_{ij}=B^{P_1}_{ijkl}\Sigma_{kl} \tag{38}$$

$$\sigma^{P_2}_{mn}=B^{P_2}_{mnop}\Sigma_{op}. \tag{39}$$

The local stress state of P_1 is related to the one of P_2 by

$$\sigma^{P_1}_{ij}=\sigma^{P_2}_{mn}T_{mi}T_{nj} \tag{40}$$

and the effective stress states are related by

$$\Sigma_{kl}=\Sigma_{op}T_{ok}T_{pl}. \tag{41}$$

After substituting the Eqs. (40) and (41) into Eq. (38) we get

$$\sigma^{P_2}_{mn}T_{mi}T_{nj}=B^{P_1}_{ijkl}\Sigma_{op}T_{ok}T_{pl}, \tag{42}$$

and solving for $\sigma^{P_2}_{mn}$ yields

$$\sigma^{P_2}_{mn}=\underbrace{B^{P_1}_{ijkl}T_{im}T_{jn}T_{ko}T_{lp}}_{B^{P_2}_{mnop}}\Sigma_{op}. \tag{43}$$

Comparing Eqs. (43) and (39) one sees that the mapping tensors $B^{\mathrm{P}_1}_{ijkl}$ and $B^{\mathrm{P}_2}_{mnop}$ for two homologous points P_1 and P_2 are similar and can be transformed into each other using

$$B^{\mathrm{P}_2}_{mnop} = B^{\mathrm{P}_1}_{ijkl} T_{im} T_{jn} T_{ko} T_{lp}, \tag{44}$$

where T_{im} describes the transformation from P_1 to P_2. To study the failure behaviour of a symmetric structure, only a single fundamental domain has to be evaluated.

Stress intensity factors (SIF) describe the local loading of a crack depending on the local stress state at the crack tip, see [25]

$$\begin{Bmatrix} K_{\mathrm{I}} \\ K_{\mathrm{II}} \\ K_{\mathrm{III}} \end{Bmatrix} = \lim_{r \to 0} \sqrt{2\pi r} \begin{Bmatrix} \sigma_{22}(r,\ \alpha = 0) \\ \sigma_{12}(r,\ \alpha = 0) \\ \sigma_{23}(r,\ \alpha = 0) \end{Bmatrix} \tag{45}$$

defined in a local crack tip coordinate system as shown in Fig. 7 (left). Because of the proportionality of

$$K_N \sim \sigma_{ij} \sim \Sigma_{kl} \tag{46}$$

the SIF can be calculated using

$$K_N = D^{P}_{Nkl} \Sigma_{kl} \tag{47}$$

analogous to Eq. (37) for a linear elastic problem with D^{P}_{Nkl} as the mapping tensor from the effective stress state to the SIFs for a point P at the crack tip. Two mapping tensors $D^{\mathrm{P}_1}_{Nkl}$ and $D^{\mathrm{P}_2}_{Nmn}$ of two homologous points P_1 and P_2 can be transformed into each other using, analogous to Eq. (44)

$$D^{\mathrm{P}_2}_{Nmn} = D^{\mathrm{P}_1}_{Nkl} T_{km} T_{ln}. \tag{48}$$

Also for the evaluation of the SIFs, a single fundamental domain needs to be investigated only. An example for the crack paths of a single fundamental domain is shown in Fig. 7 (right). Analogously, the failure tensors (see Eq. 34) of two homologous points $A^{\mathrm{P}_1}_{ijkl}$ and $A^{\mathrm{P}_2}_{mnop}$ can be transformed into each other using

$$A^{\mathrm{P}_2}_{mnop} = A^{\mathrm{P}_1}_{ijkl} T_{im} T_{jn} T_{ko} T_{lp}. \tag{49}$$

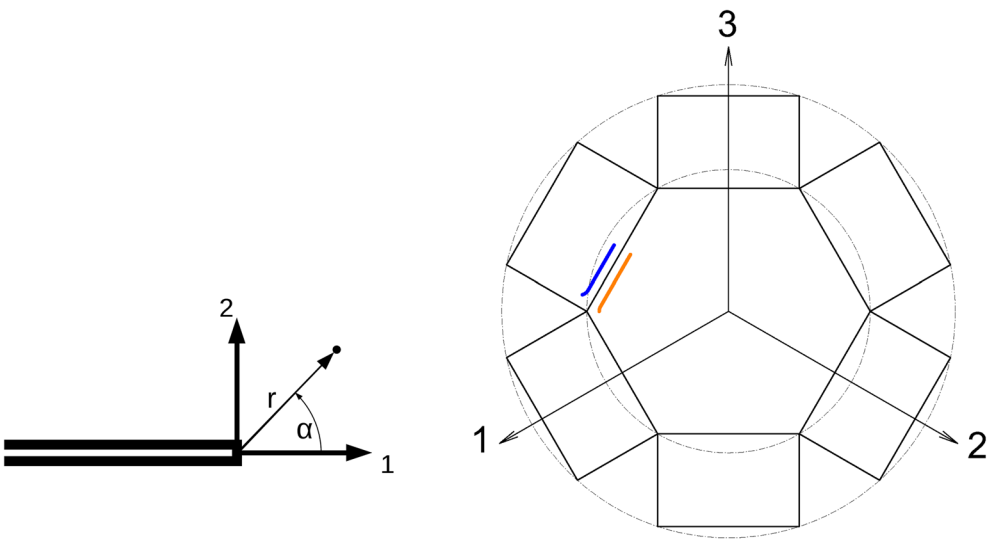

Fig. 7 (*Left*) Local Cartesian and cylindrial coordinate systems at crack tip. (*Right*) Crack paths of fundamental domain

3 Results

3.1 Results for homologous points

At the top of Fig. 8, an outline of a part of the Kelvin cell model is shown where the locations of four homologous points are indicated. Under the same effective loading, two homologous points can have the same magnitude of the local stress σ_{ij} but the sign can be different if the corresponding domains have a mirror symmetry. For an uniaxial loading in the 3-direction, all domains have a symmetric local stress σ_{33} with the same sign of the local stress. For a shear loading in (12)-direction, mirroring with respect to the (13)-plane changes the sign of σ_{13} but mirroring with respect to the (23)-plane does not. For these homologous points, the magnitudes of σ_{33} and σ_{13} are constant.

In a second example we change the effective stress state from a uniaxial $\Sigma_{11} = 1/16\,\text{MPa}$ to an uniaxial stress state with $\Sigma_{22} = 1/16\,\text{MPa}$. This is equivalent to a rotation of the stress state around the (111)-axis by an angle $\alpha = 2/3\,\pi$. In Fig. 9 the results of the two effective stress states are shown. Left the local σ_{11} stresses are shown and right the local σ_{22} stresses. The results are the same except for a rotation of $2/3\,\pi$ around the (111)-axis.

A similar result is obtained, if we look at local von Mises stresses as it is shown in Fig. 10.

As an example for the mirror and point symmetries of the SIF, the four-sided strut loop around the normal (001) under effective shear loading Σ_{13} is investigated in Fig. 11. We find one set of homologous points

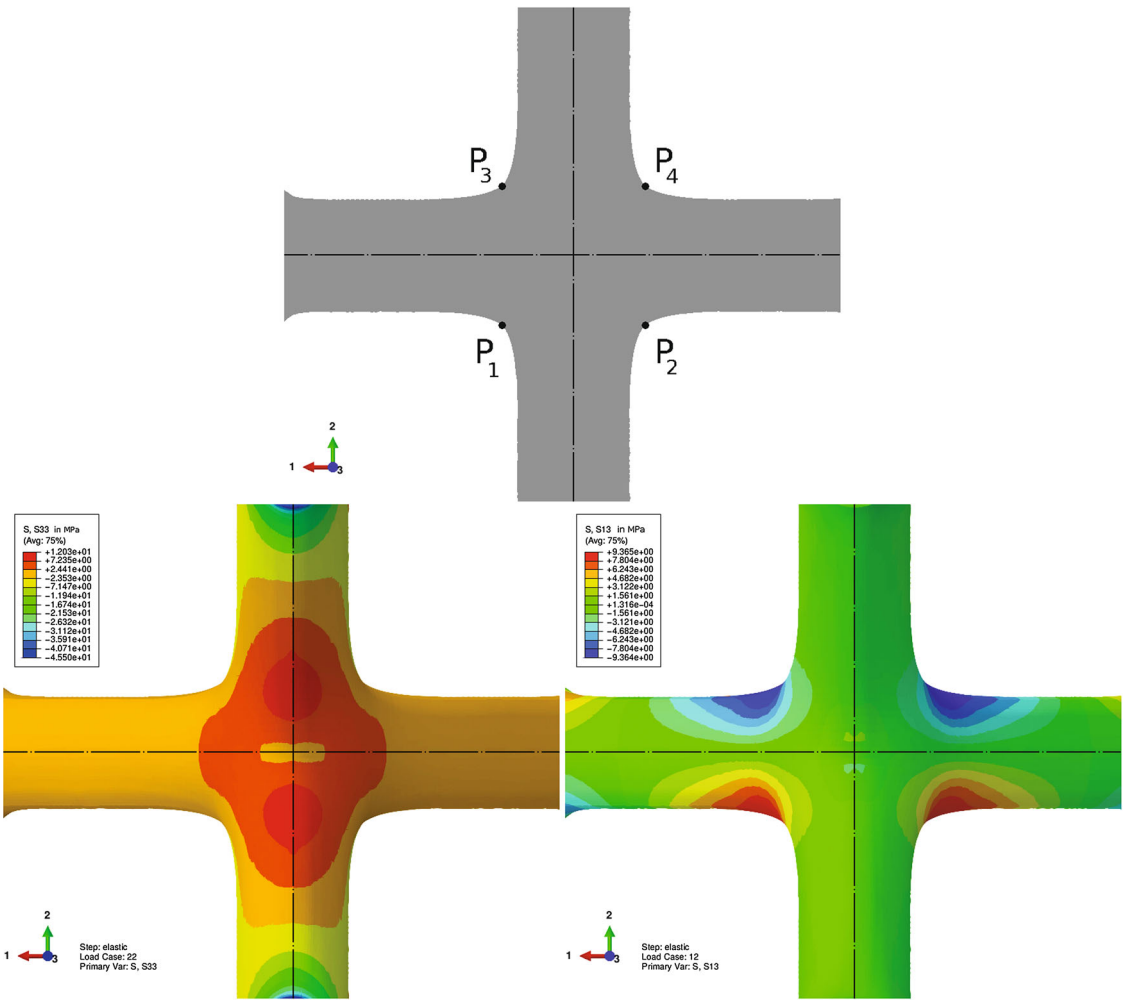

Fig. 8 (*Top*) Location of four homologous points. (*Left*) Local stresses σ_{33} (in MPa) under effective uniaxial loading $\Sigma_{22} = 1/16\,\text{MPa}$. (*Right*) Local stress σ_{13} (in MPa) under effective shear loading $\Sigma_{12} = 1/16\,\text{MPa}$

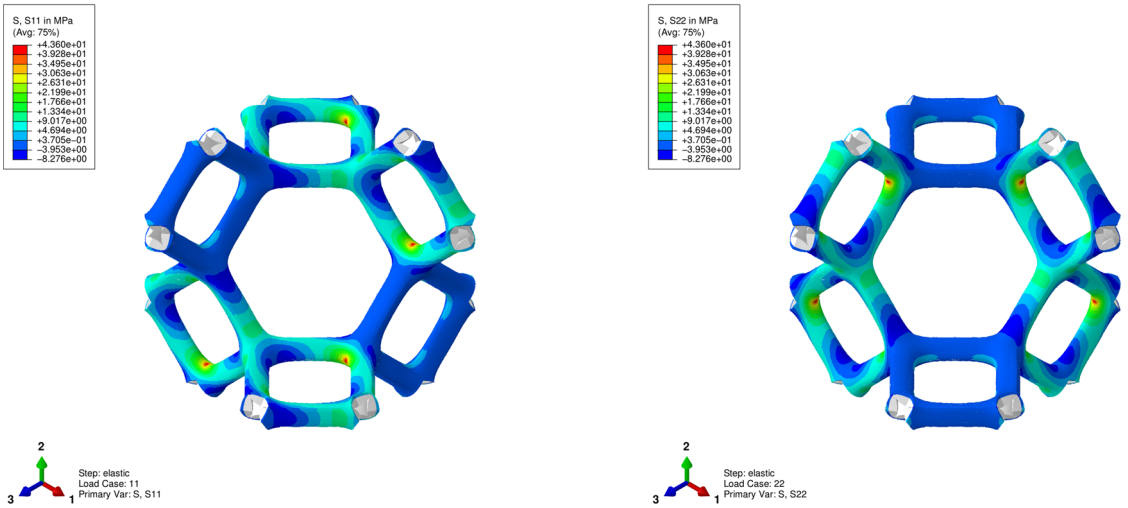

Fig. 9 (*Left*) Local stress σ_{11} (in MPa) under effective uniaxial loading $\Sigma_{11} = 1/16\,\text{MPa}$. (*Right*) Local stress σ_{22} (in MPa) under effective uniaxial loading $\Sigma_{22} = 1/16\,\text{MPa}$

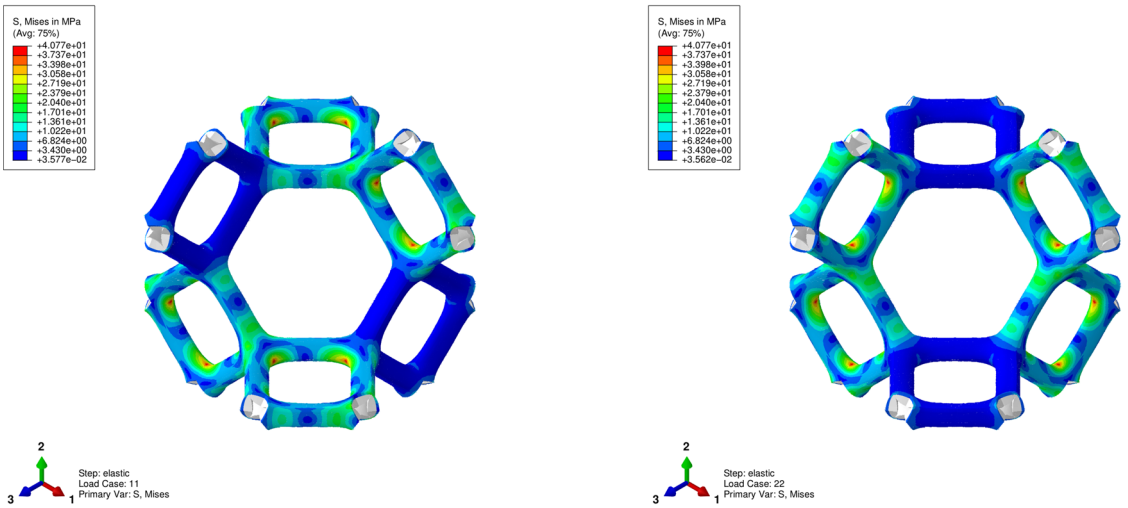

Fig. 10 Values of von Mises failure criteria of two uniaxial effective loadings, (*left*) $\Sigma_{11} = 1/16\,\text{MPa}$, (*right*) $\Sigma_{22} = 1/16\,\text{MPa}$

at the local parametric coordinates lpc $= [0, 1, 2, 3]$ and second set at lpc $= [0.5, 1.5, 2.5, 3.5]$. The graph for K_{II} has mirror symmetries at lpc $= [1.5, 3.5]$ and point symmetries at lpc $= [0.5, 2.5]$. The K_{III} graph instead has mirror symmetries at lpc $= [0.5, 2.5]$ and point symmetries at lpc $= [1.5, 3.5]$. A remarkable result is also that K_{I} is zero everywhere on this strut loop for a Σ_{13} loading.

3.2 Effective failure surface

The effective failure surface (EFS) for the whole foam is the minimum of the failure surfaces of all local points for the same parameters $\phi, \psi, \omega, p, q, \theta$. In Fig. 12, the failure surfaces are shown for two criteria $\lambda_{\text{vM}}(\hat{\Sigma}_{ij}) = 0$ and $\lambda_{\text{co}}(\hat{\Sigma}_{ij}) = 0$ for the basic orientation O_1, see Table 1 for the values of ϕ, ψ and ω corresponding to the rotations. Each failure surface for a single point is a quadric in the six dimensional stress space. The curves in Fig. 12 are therefore projections of those quadrics onto the two-dimensional stress plane spanned by the effective von Mises stress q and the effective hydrostatic stress p. We show the failure surfaces for a selection of six points P_1 to P_6, which are the points that become critical within our finite element discretization. The EFS is not smooth, because it is build up by intersecting quadrics.

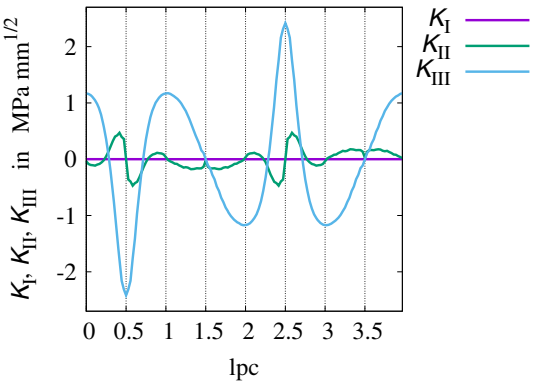

Fig. 11 SIF at the four-sided strut loop around the normal (001) under effective shear loading $\Sigma_{13} = 1/16\,\mathrm{MPa}$

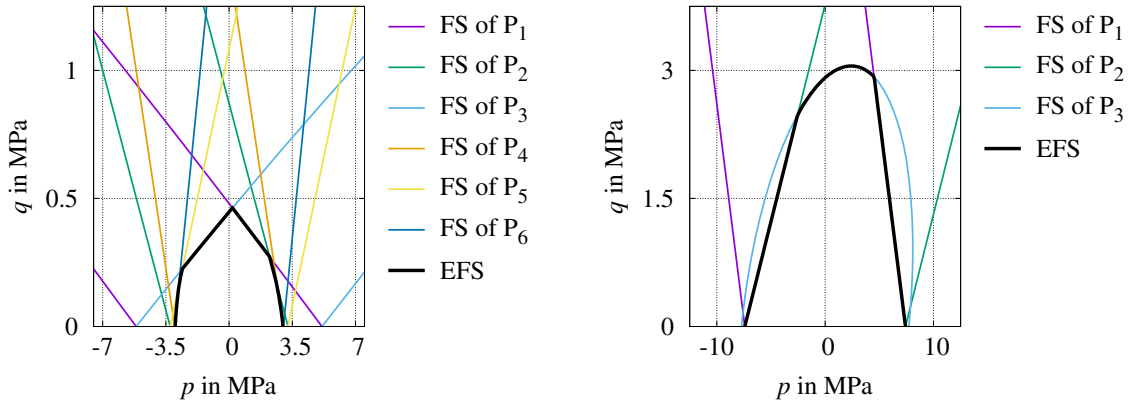

Fig. 12 Effective failure surfaces (EFS) for the orientation O_1 and $\theta = 0$ with failure surfaces (FS) of different local points P_i, (*left*) von Mises criterion $\lambda_{\mathrm{vM}}(\hat{\Sigma}_{ij}) = 0$, (*right*) coplanar stress intensity factor criterion $\lambda_{\mathrm{co}}(\hat{\Sigma}_{ij}) = 0$

Table 1 Parameters of stress state orientations of ϕ, ψ and ω used for Figs. 12 and 13

	O_1	O_2	O_3	O_4	O_5	O_6
ϕ	0	0	$\phi_{\max}$	$\phi_{\max}$	$\phi_{\max}$	$\phi_{\max}$
ψ	0	0	0	0	$\psi_{\max}$	$\psi_{\max}$
ω	0	$\frac{\pi}{4}$	0	$\frac{\pi}{4}$	0	$\frac{\pi}{4}$

Since the Kelvin cell is not isotropic, the orientation of the stress state has an influence on the shape of the failure surfaces if they are plotted in the q-p-plane. Figure 13 shows the EFS of $\lambda_{\mathrm{vM}}(\hat{\Sigma}_{ij}) = 0$ and $\lambda_{\mathrm{co}}(\hat{\Sigma}_{ij}) = 0$ for three different Lode angles θ and the six orientations, which are defined by the angles ϕ, ψ and ω as listed in Table 1. For pure hydrostatic stress states, the orientation does not influence the results, so the intersection points of the EFS with the hydrostatic axis are equal.

For a Lode angle of $\theta = 0$, a rotation with ω has no effect on the EFS for both criteria λ_c. For Lode angles $\theta \neq 0$, the results depend strongly on ϕ, ψ and ω. For rather low hydrostatic stresses the smallest values for the EFS are found either for the first O_1 or third O_3 orientation of the stress states for both investigated failure criteria. If the stress state is nearly hydrostatic other orientations can become critical.

All failure surfaces, four our chosen two criteria, are point symmetric with regard to the stress space origin, which can be expressed by $\lambda_c(p, q, \theta, \phi, \psi, \omega) = \lambda_c(-p, q, \theta + \pi, \phi, \psi, \omega)$.

If we compare the two EFSs in Figs. 12 and 13, we see that all values for the coplanar criterion $\lambda_{\mathrm{co}}(\hat{\Sigma}_{ij}) = 0$ are greater than the values for the von Mises criterion $\lambda_{\mathrm{vM}}(\hat{\Sigma}_{ij}) = 0$. That means that for the given geometry, relative density and the given material parameter set the structure would rather fail due to high stresses at the strut surfaces according to stretching, bending and torsion. The sharp-edged cavities seem to be uncritical, at least for the given configuration.

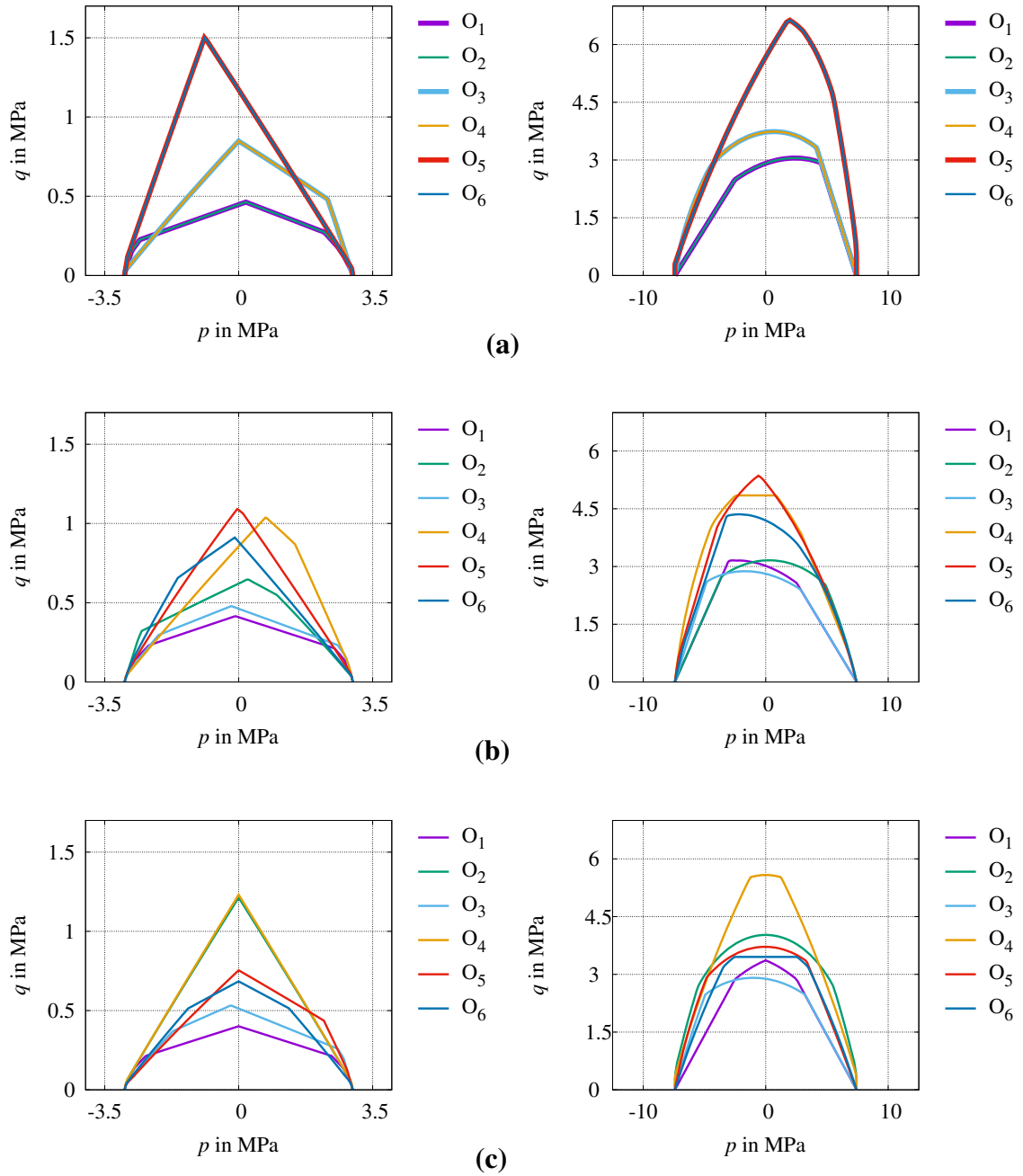

Fig. 13 Effective failure surfaces for three different Lode angles θ, (*left*) von Mises criterion $\lambda_{\mathrm{vM}}(\hat{\Sigma}_{ij}) = 0$, (*right*) coplanar stress intensity factor criterion $\lambda_{\mathrm{co}}(\hat{\Sigma}_{ij}) = 0$

4 Conclusions

A method is presented to model reticulated open cell ceramic foams containing sharp edges cavities. For such structures, stress intensity factors can be calculated for effective multi-axial loadings. The presented tools can be used for arbitrary open cell foam structures.

Effective failure surfaces for inhomogeneous structures are defined as the minimum of the failure surfaces of all local points of the structure under consideration. Since the Kelvin cell obeys octahedral symmetries only a single fundamental domain needs to be considered to compute the EFS of the whole structure. The local stress states and therefore stress-based local failure criteria of two homologous points in two different

fundamental domains can be transformed into each other only by knowing the relative spatial orientation of the two fundamental domains. Since the octahedral symmetry group contains 48 elements (transformation matrices), the costs for computational post-processing can be reduced to 1/48.

The inspection of the EFSs for the von Mises criterion as well as for the coplanar 3D Mixed-Mode fracture criterion are anisotropic for a Kelvin cell under multi-axial mechanical loading. Since both criteria are point symmetric, the EFSs also show this feature. It should be pointed out that the current simulations allow negative K_{I} values, without checking if the crack faces are intersecting each other. Therefore, contact models need to be implemented. Then negative K_{I} values would influence the K_{II} and K_{III} values due to friction between the crack faces.

All EFSs for the 3D Mixed-Mode fracture criterion are obtained for larger stresses than the effective failure surfaces for the von Mises criterion. This means that for the given geometry, relative density and the given material parameter set the structure would rather fail due to high stresses at the strut surfaces according to stretching, bending and torsion. The sharp-edged cavities seem to be uncritical, at least for the given configuration. It is uncertain if the edges of the cavities can be more critical for another geometry of the ceramic foam.

The investigations presented in this paper were done only for mechanical loading. With the presented tools, the stress intensity factors can be calculated also for thermo-mechanical loadings, especially for thermal shocks, which occur if the foams are used as filters in metal melt filtration applications.

Acknowledgments The authors gratefully acknowledge the financial support by the German Research Foundation (DFG) within the collaborative research centre SFB 920.

References

1. Schwartzwalder, K.: Method of making porous ceramic articles, US patent 3,090,094 (1963)
2. Colombo, P., Hellmann, J.R.: Ceramic foams from preceramic polymers. Mater. Res. Innov. **6**(5–6), 260–272 (2002). doi:10.1007/s10019-002-0209-z
3. Twigg, M., Richardson, J.: Theory and applications of ceramic foam catalysts. Chem. Eng. Res. Des. **80**(2), 183–189 (2002). doi:10.1205/026387602753501906
4. Gibson, L.J., Ashby, M.F.: Cellular Solids. Cambridge Solid State Science Series. Cambridge University Press, Cambridge (1999)
5. Jang, W.-Y., Kraynik, A.M., Kyriakides, S.: On the microstructure of open-cell foams and its effect on elastic properties. Int. J. Solids Struct. **45**(7–8), 1845–1875 (2008)
6. Kraynik, A.M., Reinelt, D.A., van Swol, F.: Structure of random monodispersed foam. Phys. Rev. E **67**, 0314031/1–0314031/4 (2003). doi:10.1103/PhysRevE67.031403
7. Brakke, K.A.: The surface evolver. Exp. Math. **1**(2), 141–165 (1992)
8. Storm, J., Abendroth, M., Zhang, D., Kuna, M.: Geometry dependent effective elastic properties of open-cell foams based on Kelvin cell models. Adv. Eng. Mater. **15**(12), 1292–1298 (2013)
9. Thomson, W.: On the division of space with minimum partitional area. Philos. Mag. **24**(151), 503 (1887)
10. Mills, N., Gilchrist, A.: High strain extension of open-cell foams. J. Eng. Mater. Technol. **122**(1), 67–73 (1999). doi:10.1115/1.482767
11. Dement'ev, A., Tarakanov, O.: Effect of cellular structure on the mechanical properties of plastic foams. Polym. Mech. **6**(4), 519–525 (1970)
12. Dement'ev, A., Tarakanov, O.: Model analysis of the cellular structure of plastic foams of the polyurethane type. Polym. Mech. **6**(5), 744–749 (1970)
13. Gong, L., Kyriakides, S., Triantafyllidis, S.: On the stability of Kelvin cell foams under compressive loads. J. Mech. Phys. Solids **53**(4), 771–794 (2005)
14. Zhu, H., Knott, J., Mills, N.: Analysis of the elastic properties of open-cell foams with tetrakaidecahedral cells. J. Mech. Phys. Solids **45**, 319–343 (1997)
15. Warren, W., Kraynik, A.: Linear elastic behavior of a low-density kelvin foam with open cells. ASME J. Appl. Mech. **64**, 787–793 (1997)
16. Deshapande, V., Fleck, N.: Isotropic constitutive models for metallic foams. J. Mech. Phys. Solids **48**, 1253–1283 (2000)
17. Bigoni, D., Piccolroaz, A.: Yield criteria for quasibrittle and frictional materials. Int. J. Solids Struct. **41**(11), 2855–2878 (2004), . http://www.sciencedirect.com/science/article/pii/S0020768303007273
18. Altenbach, H., Bolchoun, A., Kolupaev, V.: Phenomenological yield and failure criteria. In: Altenbach, H., Öchsner, A. (eds.) Plasticity of Pressure-Sensitive Materials, Engineering Materials, pp. 49–152. Springer, Berlin (2014). doi:10.1007/978-3-642-40945-5_2
19. Skoge, M., Donev, A., Stillinger, F., Torquato, S.: Packing hard spheres in high dimensional Euclidean spaces. Phys. Rev. E **74**, 041127 (2006)
20. Rycroft, C.: Voro++: a three dimensional voronoi cell library in C++. Chaos **19**, 041111 (2009)
21. Systèmes, D.: Abaqus 6.12 Theory Manual. Dassault Systèmes Simulia Corp., Providence (2012)
22. Munz, D., Fett, T.: Ceramics: Mechanical Properties, Failure Behaviour, Materials Selection, vol. 36. Springer Science & Business Media, Berlin (1999)

23. Suresh, S., Shih, C., Morrone, A., O'Dowd, N.: Mixed-mode fracture toughness of ceramic materials. J. Am. Ceram. Soc. **73**(5), 1257–1267 (1990)
24. Rice, J.R.: A path independent integral and the approximate analysis of strain concentration by notches and cracks. ASME J. Appl. Mech. **35**(2), 379–386 (1968)
25. Kuna, M.: Finite Elements in Fracture Mechanics. Springer, Berlin (2013)